

Hardware optimized parity check gates for superconducting surface codes

Matthew J. Reagor¹, Thomas C. Bohdanowicz², David Rodríguez Pérez¹,
Eyob A. Sete¹, and William J. Zeng²

¹Rigetti Computing, Berkeley, CA 94710

²Goldman, Sachs & Co., New York, NY

November 11, 2022

Error correcting codes use multi-qubit measurements to realize fault-tolerant quantum logic steps. In fact, the resources needed to scale-up fault-tolerant quantum computing hardware are largely set by this task. Tailoring next-generation processors for joint measurements, therefore, could result in improvements to speed, accuracy, or cost—accelerating the development large-scale quantum computers. Here, we motivate such explorations by analyzing an unconventional surface code based on multi-body interactions between superconducting transmon qubits. Our central consideration, Hardware Optimized Parity (HOP) gates, achieves stabilizer-type measurements through simultaneous multi-qubit conditional phase accumulation. Despite the multi-body effects that underpin this approach, our estimates of logical faults suggest that this design can be at least as robust to realistic noise as conventional designs. We show a higher threshold of 1.25×10^{-3} compared to the standard code’s 0.79×10^{-3} . However, in the HOP code the logical error rate decreases more slowly with decreasing physical error rate. Our results point to a fruitful path forward towards extending gate-model platforms for error correction at the dawn of its empirical development.

1 Introduction

Surface codes [Bravyi and Kitaev, 1998, Dennis et al., 2002, Fowler et al., 2012] and related methods for stabilizer quantum error correction on 2D lattices [Bravyi et al., 2012, Terhal, 2015, Li et al., 2019] are leading candidates for large-scale quantum computers based on solid-state platforms, such as superconducting qubits. As these types of processors demonstrate increasingly sophisticated error correction protocols [Kelly et al., 2015, Andersen et al., 2020, Marques et al., 2021, Chen et al., 2021, Krinner et al., 2022], the opportunity to tailor code design to superconducting hardware [Michael et al., 2016, Tuckett et al., 2018] and vice-versa [Mirrahimi et al., 2014, Royer et al., 2018, Chamberland et al., 2022] promises to accelerate progress towards fault-tolerant algorithms. Indeed, specialisation has already played an important role in this respect—the first bit-flip correction mechanisms on superconductors leveraged a non-standard Toffoli gate [Reed et al., 2012], and achieving break-even error rates between physical and logical qubits for superconductors relied on an auxiliary memory to the transmon qubit [Ofek et al., 2016]. Yet, hardware that has been purpose-made for error correction is not necessarily also optimal for studying near-term quantum algorithms¹. As a consequence, systems that have been scaled-up to the order of one-hundred qubits, to date, are exclusively gate-model devices based on planar superconducting transmon circuits.

Motivated by progress extending the reach of these gate-model platforms with application-specific logic—including gates for chemistry [Foxen et al., 2020], many-body complex systems [Blok

Matthew J. Reagor: matt@rigetti.com

Thomas C. Bohdanowicz: thom.bohdanowicz@gs.com

¹such as variational quantum-classical methods [Cerezo et al., 2021]

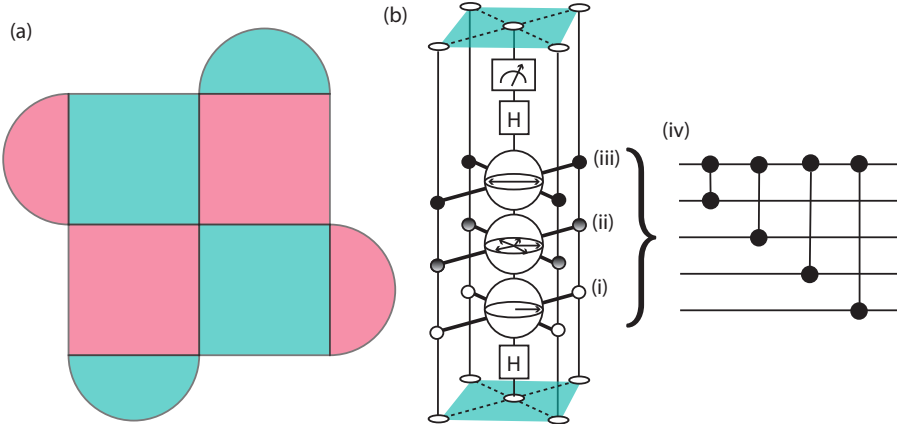


Figure 1: Concept surface code design. (a) A small patch of rotated surface code with Z-checks shown in teal and X-checks shown in magenta. Data qubits are located at the vertices of the tessellation with a single stabilizer check qubit within each tile. (b) Performing a Z-check with the Hardware-Optimized Parity (HOP) gate. Dashed lines on this square indicate the presence of pairwise dispersive ZZ interaction between the stabilizer check qubit, located at the center of the square, and the four data qubits, located at the vertices. The Z-check protocol begins with an unconditional Hadamard gate applied to the stabilizer check qubit preparing the qubit along the X-axis of its Bloch sphere. Activating the gate and evolving the five-qubit system under the interaction Hamiltonian accumulates the desired phase gate, wherein at (i) no entanglement is present, (ii) phase collapse, (iii) register parity mapped to the $\pm X$ states of the check qubit. The time evolution (i-iii) is equivalent to the four CZ circuit shown in (iv). Finally, a second unconditional Hadamard gate rotates the check qubit to the measurement Z basis. The sequence for X -checks is equivalent up to additional Hadamard gates on the data qubits before and after the sequence shown for Z-checks.

et al., 2021], and optimization [Lacroix et al., 2020, Hill et al., 2021]—we ask whether contemporary superconducting processors can be tailored for performing efficient stabilizer quantum error correction. Such a strategy would reduce the requirements for fault-tolerance while taking advantage of the significant investment towards machines for near-term quantum applications. While other recent advances in optimizing the surface code have focused on using qubit pair measurements to eliminate the use of two-qubit entangling gates [Gidney, 2022, Chao et al., 2020], we take a different approach by implementing a single five-qubit entangling gate. Notably, ion traps have successfully utilized a native multi-qubit gate, the Mølmer-Sørensen (MS) gate [Mølmer and Sørensen, 1999], for efficient stabilizer measurements in error correction experiments [Erhard et al., 2021, Nigg et al., 2014]. Moreover, there is numerical evidence that error correction thresholds do not suffer from the more complex noise associated with the multi-qubit MS gate [Bermudez et al., 2017, Schwerdt et al., 2022].

In the following, we show how to adapt the control of contemporary gate-model superconducting processors to achieve a different error profile, relative to standard quantum circuit constructions. Our superconducting processor layout is based on planar transmons arranged in a square array with one qubit coupled to four nearest-neighbors via tunable couplers, which is a leading design for near-term processors [Arute et al., 2019, Foxen et al., 2020, Sung et al., 2021, Sete et al., 2021]. To operate the chip for error correction (see Fig. 1), exchange coupling rates and qubit frequencies are tuned to engineer a strong-dispersive ZZ interaction pairwise between data qubits and local stabilizer check qubits constant during the gate². Evolved over time, the interaction generates a Hardware Optimized Parity (HOP) gate, controlled on the data register and targeting a local stabilizer check qubit—mapping the odd and even parity states of the register onto two states of the stabilizer check qubit. Measuring the stabilizer qubit then records the associated error syndrome. The HOP-based design reduces the system calibration problem to a single gate per check.

Our analysis considers HOP gates performing the surface codes with a realistic noise model

²This interaction is the dual of the MS gate for ions, which is generated by an XX interaction [Mølmer and Sørensen, 1999]. We therefore anticipate that related analysis of MS-based codes [Bermudez et al., 2017, Schwerdt et al., 2022] will carry over to a large degree.

that captures incoherent errors, measurement errors, as well as spurious next-nearest neighbor Hamiltonian terms. Numerical simulations indicate that the HOP surface code does not correct the same number of errors as a traditional surface code with optimized CNOT schedule. Surprisingly, however, the HOP design may have error correction advantages for near-term machines due to a higher threshold. As a result, we estimate modest physical overhead reductions (15%) are possible, for example, at the scale needed for a target application in pricing financial derivatives [Chakrabarti et al., 2021].

This manuscript is organized into three technical sections. First, we show how a superconducting processor being developed for gate-model applications can be tuned to support efficient HOP gates. Second, we discuss the associated device noise model for a HOP gate. Finally, we analyze the performance of rotated surface codes mediated by HOP gates, relative to standard constructions.

2 Superconducting Processor Design

In the following section, we discuss the physical mechanisms underpinning the HOP gate using superconducting qubits. This includes both a micro-architecture based on transmon circuits with tunable couplers as well as system design considerations towards heat dissipation. Overall, we seek to realize a five-qubit HOP gate via a pairwise dispersive interaction between a single stabilizer qubit and four local data qubits with equal coupling strength,

$$H_{\text{disp}} = \frac{-\zeta(t)}{4} \sum_{k=1}^4 Z_0 Z_k, \quad (1)$$

where $\zeta(t)$ is a time-dependent interaction strength (described in more detail soon), Z_k is the Pauli-Z operator acting on the k -th qubit, with the index $k = 0$ assigned to the stabilizer check qubit. Allowing the five-qubit system evolve under this Hamiltonian with a constant interaction strength ζ_0 for a time $\tau = \pi/\zeta_0$ corresponds to applying a total unitary $U = \exp\{i\pi/4 \sum_k Z_0 Z_k\}$ which is equivalent to the four CZ gate construction shown in Fig. 1 up to single-qubit phase gates applied to the data qubits (\sqrt{Z} rotations on each). Within a protocol for Z -stabilizer measurements (see Fig.1), the system is biased with no interactions ($\zeta(0) = 0$), and in this configuration, stabilizer qubits are prepared along the X -axis via Hadamard (H) gates. After turning on the interaction and waiting an amount τ , the interaction is turned off $\zeta(t \geq \tau) = 0$. A final Hadamard gate maps the state of the stabilizer qubit as $\langle Z_0 \rangle = -1$ for even number of excited data qubits, and $\langle Z_0 \rangle = +1$ for odd. Thus, HOP gates enable a single-operation parity check on the four data qubits. For the typical gate-model configurations we consider here, estimates of $\zeta/2\pi = 5$ MHz corresponds to a HOP gate time of $\tau = 100$ ns. Measuring X -stabilizers instead has H gates applied to the data qubits but otherwise follows the same protocol.

The Hamiltonian (1) can be realized by coupling the stabilizer qubit to the data qubits using a tunable coupler, following the schematic approach shown in Fig. 2. In this design, we utilize the asymmetric tunable coupler introduced in Sete et al. [2021]. For this type of coupler the zero-coupling condition is achieved by placing the tunable coupler frequency above that of the qubits. The qubit-qubit coupling can be varied from $\zeta = 0$ to the target coupling ζ_0 by tuning the flux bias of the tunable coupler. In gate-model operation, the couplings between the qubits are turned on and off to actuate two-qubit entangling gates. However, here we activate multiple couplings simultaneously.

Following Sete et al. [2021], the five qubit and four tunable coupler system can be described by

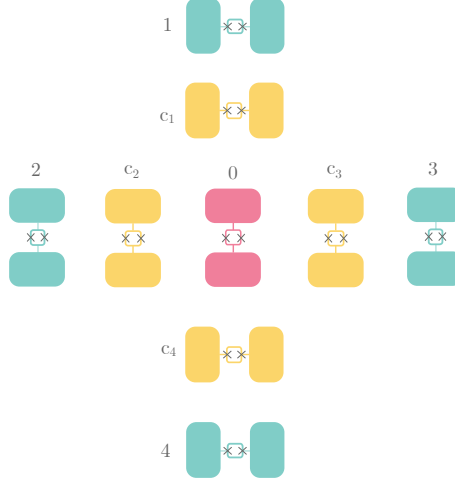


Figure 2: Schematic of a 5-qubit lattice for four-qubit parity check measurement. Stabilizer qubit (magenta) is coupled to four data qubits (teal) via asymmetric floating tunable couplers c_j (yellow) introduced in Ref. [Sete et al. \[2021\]](#).

the following Hamiltonian with a three-level approximation for each anharmonic mode

$$\begin{aligned}
 H = & \sum_{j=0}^4 \omega_j(\Phi_j) |1\rangle_j \langle 1| + (2\omega_j(\Phi_j) - \eta_j(\Phi_j)) |2\rangle_j \langle 2| \\
 & + \sum_{k=1}^4 \omega_{c_k}(\Phi_k) |1\rangle_{c_k} \langle 1| + [2\omega_{c_k}(\Phi_k) - \eta_{c_k}(\Phi_k)] |2\rangle_{c_k} \langle 2| \\
 & + \sum_{m=1}^4 [g_{0m} X_0 X_m + g_{0c_m} X_0 X_{c_m} + g_{mc_m} X_m X_{c_m}], \tag{2}
 \end{aligned}$$

where ω_j and η_j are the j th qubit frequency and anharmonicity; ω_{ck} and η_{ck} are frequency and anharmonicity of the k th tunable coupler, g_{0m} , ($m \in [1, 4]$) are the direct stabilizer qubit-data qubit couplings, g_{0c_m} ($m \in [1, 4]$) are the stabilizer qubit-tunable coupler couplings, and g_{mc_m} ($m \in [1, 4]$) are the data qubit-tunable coupler couplings. Here $X_j = \sigma_{-,j} + \sigma_{+,j}$, where $\sigma_{-,j} = |0\rangle_j \langle 1| + \sqrt{2}|1\rangle_j \langle 2|$ is the lowering operator for the j th qubit or coupler. We assume the qubits and tunable couplers are flux tunable transmon qubits and their frequencies as a function of the flux bias can be approximated by

$$\omega_m(\Phi_m) = \sqrt{8E_{\text{Jeff},m}E_{C,m}} - E_{C,m}(1 + \xi_m/4 + 21\xi_m^2/128), \tag{3}$$

$$\eta_m(\Phi_m) = E_{C,m}(1 + 9\xi_m/16 + 81\xi_m^2/128), \tag{4}$$

$$E_{\text{Jeff},m} = \frac{E_{J,m}}{1 + r_m} \sqrt{1 + r_m^2 + 2r_m \cos(2\pi\Phi_m/\Phi_0)}, \tag{5}$$

where $m \in \{[1, 4], [c_1, c_4]\}$, $\xi_m = \sqrt{2E_{C,m}/E_{\text{Jeff},m}}$ and $r_m = E_{J1,m}/E_{J2,m}$ is the ratio of the junction energies, $E_{J1,m}, E_{J2,m}$ of the SQUID, $E_{C,m}$ is the charging energy, and $E_{J,m} = E_{J1,m} + E_{J2,m}$ is the total junction energy; Φ_m and Φ_0 are the external flux bias and flux quantum, respectively. Note that the qubit-coupler couplings g_{0c_m} and g_{mc_m} depend on the external flux biases Φ_m . Explicit dependence of the these couplings are used when computing the nearest neighbor ($Z_0 Z_k$) and next-nearest neighbor ($Z_{j \neq 0} Z_k$) couplings. The designed operating point assumes flux-biasing to adjust all qubits to their maximum frequencies and all tunable couplers to their minimum frequencies ($\Phi_k = 0.5\Phi_0$) in order to maximize the dispersive stabilizer-data qubit couplings while keeping the $Z_{j \neq 0} Z_k$ coupling minimum, although small bias adjustments are anticipated to account for fabrication tolerances.

We estimate the coupling strengths numerically by exact diagonalization of the Hamiltonian comprising three energy levels for each of the five transmons and four tunable couplers (3^9 dimensions), on a workstation with 256 GB of RAM and 128 CPU cores. We identify the dispersive

coupling strengths for each interaction as the frequency difference,

$$\zeta_{jk} = \omega_{|11\rangle_{jk}} + \omega_{|00\rangle_{jk}} - \omega_{|10\rangle_{jk}} - \omega_{|01\rangle_{jk}} \quad (6)$$

where $\omega_{|nm\rangle_{jk}}$ is the eigenfrequency associated with n (m) excitations in the j -th (k -th) mode and $-\zeta_{jk}/4$ is the weight of the $Z_j Z_k$ term in the interaction Hamiltonian as in Eq. 1. For realistic parameters for asymmetric tunable couplers and qubits (shown in Table 1 and Table 2), we find that $\zeta_{0k}/2\pi = 5.0$ MHz and $\zeta_{jk}/2\pi = 2 - 24$ kHz for $j \neq 0$. These parameters are used for the construction of the following error model and subsequent fault-tolerant analysis.

3 Error Model

We set out to provide a realistic description of the noise model associated with the HOP gate that is compatible with fault-tolerant analysis. A noisy quantum process can be described as a superoperator $\mathcal{E}(\rho)$ that takes an initial density matrix ρ to a final density matrix [Nielsen and Chuang, 2000]. Here, we are interested in describing the error channels associated with the HOP gate, rather than the more cumbersome description of the full process itself. We therefore write our circuit as the composition of the ideal unitary channel U and an error channel Λ :

$$\boxed{\mathcal{E}(\rho)} = -\boxed{U} \boxed{\Lambda}$$

with time proceeding from left to right. Formally, that basis change is conducted via:

$$\mathcal{E}(\rho) = \Lambda \circ U(\rho) = \sum_{i,j=0}^{d^2-1} \chi_{ij}^\Lambda \mathcal{P}_i U \rho U^\dagger \mathcal{P}_j^\dagger, \quad (7)$$

where χ^Λ is an error process matrix [Korotkov, 2013]; and $\{\mathcal{P}_k\}$ are elements of the multi-qubit Pauli operators, $\mathcal{P}_k \in \{I, X, Y, Z\}^{\otimes n}$. This allows us to look at errors in an interaction picture. For instance, the ideal unitary channel: $\mathcal{E}(\rho) = U \rho U^\dagger$ has only one non-zero element $\chi_{00}^\Lambda = 1$ with $\mathcal{P}_{00} = I^{\otimes n}$.

To study the effect of noise in the context of HOP surface codes, where stabilizer-type simulations are desired, we include noisy single-qubit Pauli gates³ to perform Pauli-twirling of Λ [Bennett et al., 1996a,b, Geller and Zhou, 2013], with the twirled error channel denoted as $\tilde{\Lambda}$. In the twirling approximation, the twirled error process matrix $\chi^{\tilde{\Lambda}}$ is diagonal with eigenvalues p_k each of which is a real-valued number. The weight of p_k is the probability that the $\tilde{\Lambda}$ channel applies the \mathcal{P}_k rotation, instead of the desired $I^{\otimes n}$ element. Following the convention in Eq. 3, these probabilistic Pauli gates occur after the perfect unitary.

To estimate χ^Λ , we solve the Lindblad master equation (ME) [Manzano, 2020, Nielsen and Chuang, 2000] governing the HOP gate under the types of Markovian decoherence that are the main noise in superconducting qubits, namely energy loss T_1 processes and pure dephasing T_ϕ processes [Krantz et al., 2019]. These act concurrently with interaction Hamiltonian of the gate Eq. 1 to evolve the density matrix as

$$\begin{aligned} \frac{d\rho}{dt} &= -i[H, \rho] + \sum_j \left[L_j \rho L_j^\dagger - \frac{1}{2} L_j L_j^\dagger \rho - \frac{1}{2} \rho L_j L_j^\dagger \right] \\ &\equiv \mathcal{L}(t) \rho(t) \end{aligned} \quad (8)$$

where L_j are Lindblad jump operators, and \mathcal{L} is an infinitesimal generator of the evolution sometimes called the Liouvillian superoperator [Manzano, 2020, Nielsen and Chuang, 2000].

While we will soon allow for decoherence acting each of the five qubits in the HOP gate, for the time being, we consider the effect of noise on the parity check only, which can help develop an intuition for the subsequent full analysis. In this case, the Lindblad jump operators are

$$L_j \in \left\{ \sqrt{\Gamma_1} \sigma_- \otimes I^{\otimes 4}, \sqrt{\Gamma_\phi} Z \otimes I^{\otimes 4} \right\}, \quad (9)$$

³Added noise is discussed Sec. 4.

where $\Gamma_1 = 1/T_1$ and $\Gamma_\phi = 1/T_\phi$ for the parity check qubit, and $I^{\otimes 4}$ acts on the data qubit register. This single-qubit noise generates multi-qubit back-action on the data qubits. To see this, it is helpful to consider Eq. 8 in the rotating frame of the interaction Hamiltonian (Eq. 1), as

$$\tilde{\rho}(t) \equiv e^{iHt} \rho(t) e^{-iHt} \quad (10)$$

and the jump operators similarly get transformed

$$\begin{aligned} \tilde{\sigma}_-(t) &= e^{iHt} \sigma_- e^{-iHt} = \exp \left\{ -i \frac{\zeta t}{4} \sum_k Z_k \right\} \sigma_- \\ \tilde{Z}(t) &= e^{iHt} Z e^{-iHt} = Z. \end{aligned} \quad (11)$$

Energy decay of the parity check qubit generates a phase kick onto the data qubits that is time-dependent, amplifying the effect of that error in the HOP gate. On the other hand, a dephasing event commutes through the Hamiltonian during the actuation of the HOP gate, and therefore, remains a single-qubit error. Similarly, when we include single-qubit decoherence on the data qubits, energy relaxation from these qubits gives a phase kick to the parity check qubit.

We turn to numerics to solve the ME with equal decoherence rates across all qubits. Specifically, we use QuTiP [Johansson et al., 2013] to find the propagator V_t , which is a superoperator describing the full noisy channel, as $V_t(\rho(0)) = \rho(t)$, by numerically integrating the Liouvillian:

$$V_t = \mathcal{T} \exp \left\{ \int_0^t ds \mathcal{L}(s) \right\}, \quad (12)$$

where \mathcal{T} is the time-ordering operator. The time τ for the evolution is chosen such that the interaction Hamiltonian achieves the correct entangling phase ($\tau = \pi/\zeta_0$). To estimate the error process matrix χ^Λ , we perform tomography on the composite channel: $V_t \circ U^\dagger$ with U the target multi-qubit phase gate, $U = \exp\{i(\pi/4) \sum_k Z_0 Z_k\}$. Pauli twirling removes the off-diagonal terms of χ^Λ . That yields $\chi^{\tilde{\Lambda}}$, from which we obtain the weights p_k of the corresponding Pauli channels \mathcal{P}_k . Succinctly, this procedure allows us use a low-level description of our system from Eq. 1 and Eq. 12 to establish description of the error model of the form of

$$\tilde{\Lambda}_{\text{HOP}}(\rho) = \sum_{i=0}^{1023} w_i \mathcal{P}_i \rho \mathcal{P}_i, \quad \mathcal{P}_i \in \{I, X, Y, Z\}^{\otimes 5}, \quad (13)$$

which we analyze with a parameterized noise model: we take a physical error rate p for our fault-tolerance calculations given by the HOP gate time and the single-qubit decoherence rate as $p = \tau \Gamma_2$, with $\Gamma_2 = \Gamma_1/2 + \Gamma_\phi$. To reduce the simulation overhead, we make the further assumption that $\Gamma_\phi = \Gamma_1/2$ ($T_1 = T_2$), which is typical of superconducting qubits [Krantz et al., 2019], and ignore leakage states. With this approach, we can produce a more complete error model, as illustrated in Fig. 3(b) that includes energy loss and dephasing on all five qubits⁴.

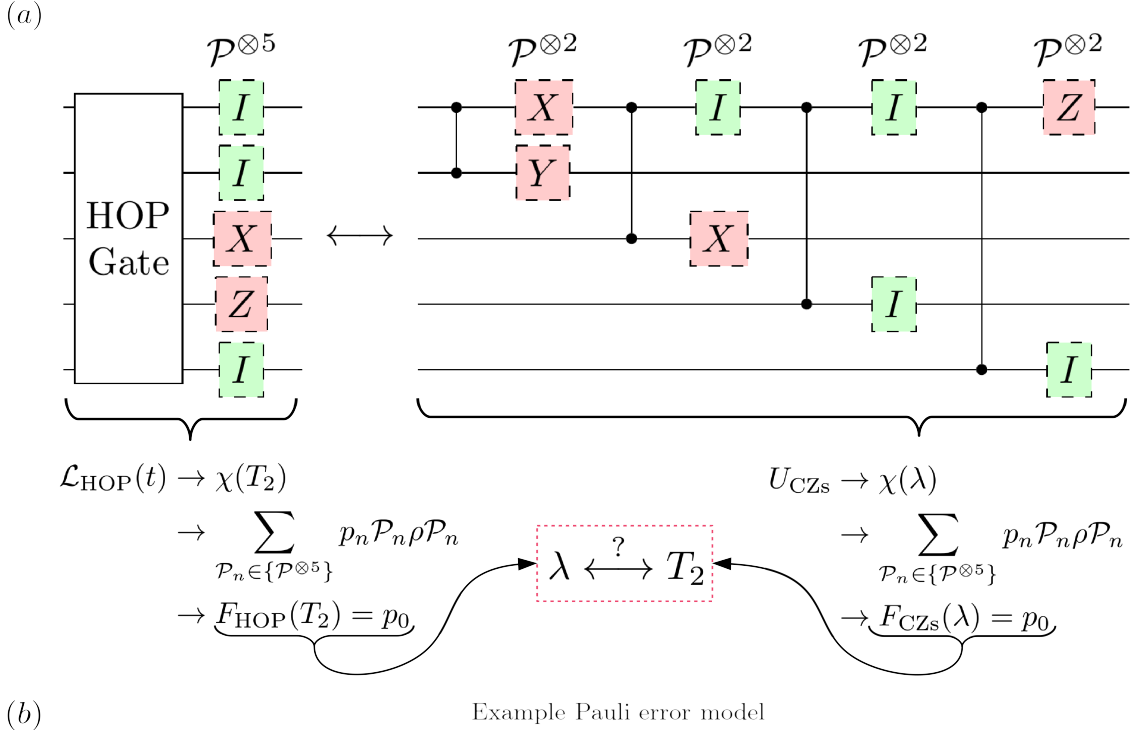
Ultimately, we are interested in understanding how the HOP gate performs in the context of error correction. Towards that end, we develop a comparison point based on a simplified quantum channel construction using the logically equivalent four CZ gates (see Fig. 1), which we call the standard construction. For the standard construction, we assume two-qubit depolarizing noise applied after each CZ gate:

$$\Delta_\lambda(\rho) = \sum_{i=0}^{15} v_i K_i \rho K_i \quad (14)$$

where the operators K_i are two-qubit Pauli operators $\mathcal{K}_i \in \mathcal{P}^{\otimes 2}$ with the corresponding weights

$$v_0 = 1 - \frac{15\lambda}{16}, \quad v_{k \neq 0} = \frac{\lambda}{16}. \quad (15)$$

⁴Additionally, we have used this framework to investigate undesired effects including the coherent ZZ cross-talk anticipated for next-nearest neighbors in Sec. 2 by adding these terms to the ME. Exploring the effects using parameters guided by simulated results (e.g. App. A), we found no discernible impact on the resulting error model and subsequent logical error threshold calculations. Thus, for simplicity, we report in the following section only results from the decoherence model.



(b) Example Pauli error model

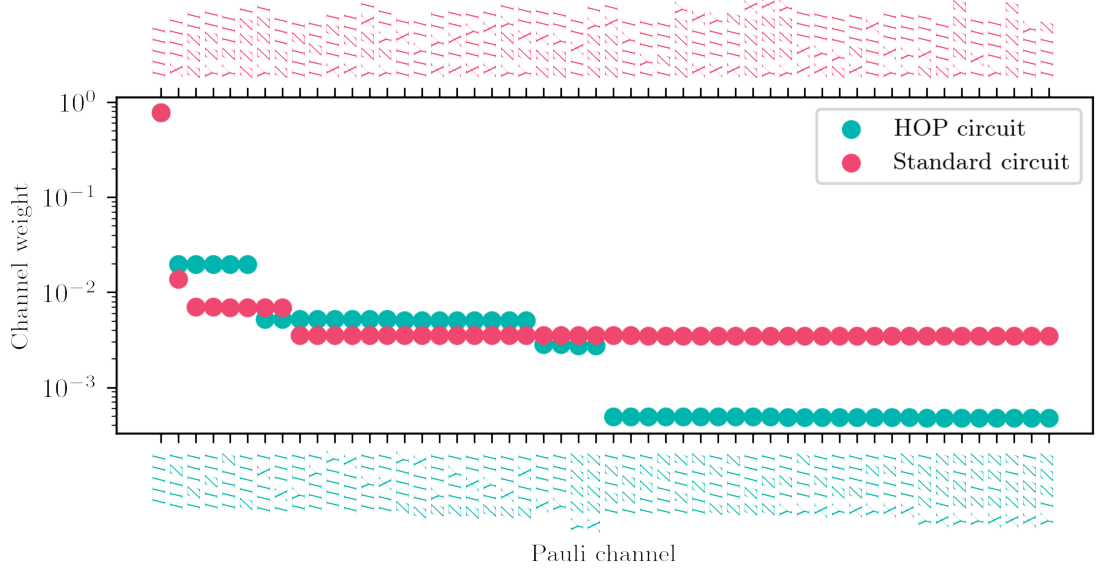


Figure 3: (a) Comparing the five-qubit Pauli error model for the HOP gate to a corresponding two-qubit depolarizing error model for the standard circuit, illustrated by an unwanted $\mathcal{P} \in \mathcal{P}^{\otimes 5}$ error for the HOP gate and unwanted $\mathcal{P} \in \mathcal{P}^{\otimes 2}$ errors after every two-qubit gate for the standard circuit. The Louivillian superoperator for a full HOP gate $\mathcal{L}_{\text{HOP}}(t)$ is used to get the error process matrix χ parameterized by coherence times T_2 , from which we get an approximated error model made up of five-qubit Paulis $\mathcal{P} = \{I, X, Y, Z\}^{\otimes 5}$. The equivalent operation made up of four CZ gates each undergoing two-qubit depolarizing noise is used to produce a superoperator process unitary U_{CZs} , from which we get the process matrix for an effective five-qubit Pauli channel parameterized by a two-qubit depolarizing rate λ . We equate the process fidelities $F_{\text{HOP}}(T_2) = F_{\text{CZs}}(\lambda)$ to determine an equivalence between λ and T_2 . (b) Resulting error models from the analysis in (a) using $\Gamma_2 = 1/T_2 = 0.05$ and a corresponding $\lambda \approx 0.066$, for channels whose weight has probability greater than 3×10^{-4} (arbitrary cutoff chosen for fitting to plot), comparing the effective error channels for both equivalent circuits. Note the process fidelities given by $IIII$ are equal.

Some of these depolarizing errors are amplified in the four CZ circuit, resulting in a non-trivial five-qubit error process matrix $\tilde{\Lambda}_{\text{CZ}}$ with an equivalent form as Eq. 3.

Recognizing that the overall process fidelity is $\tilde{\Lambda}_{\text{HOP}}^{00} = F_{\text{HOP}}(T_2)$ and $\tilde{\Lambda}_{\text{CZ}}^{00} = F_{\text{CZ}}(\lambda)$, we set $F_{\text{HOP}}(p) = F_{\text{CZ}}(\lambda)$ to determine what two-qubit depolarizing rate λ is comparable to p . Using this procedure for determining equal fidelity (used in Sec. 4 set a consistent Physical Error Rate) produces the error models in Figure 3(b), where we note that the channel weights for the Pauli $I^{\otimes 5}$ are the same. The differences in the distribution of errors across the Pauli strings illustrates the non-triviality of the relationship between these two logically equivalent processes. We observe that the most prominent Pauli channels are different between the two methods. Moreover, nearly half of Pauli channels for the HOP gate are an order of magnitude smaller than for the standard circuit, meaning the HOP based gate error may be simpler to characterize and operate in practice, a surprising potential advantage of the multi-qubit gate.

4 Error Correction Simulations

In this section, we examine fault-tolerant error correction via the rotated surface code using optimized syndrome measurement circuits based on HOP gates. In particular, we compare logical failure rates and the fault-tolerant threshold achievable using HOP syndrome measurement circuits against standard syndrome measurement circuits based on two-qubit entangling gates. We also compare resources needed for either scheme to implement a logical qubit with a target logical failure rate of $p_L = 10^{-10}$ Chakrabarti et al. [2021]. Logical failure rates are estimated via Monte Carlo simulations for a single fault-tolerant quantum error correction cycle. We empirically observe a fault-tolerant threshold for the HOP surface code that is approximately 1.5 times higher than the threshold estimated for the standard surface code. This suggests that the multi-qubit correlated error mechanisms present in the 5Q and 3Q gates are not strong enough to negatively affect the efficacy of this scheme at near-threshold error rates. We compare resource requirements for using either scheme to implement a logical qubit with logical error rate 10^{-10} and find that in regimes of interest the HOP scheme does not require greater spacetime resources than the standard scheme and may be preferable based on hardware considerations.

4.1 Parity Check Circuits and Error Models

In a typical surface code architecture, a single fault-tolerant error correction cycle is made up of d consecutive rounds of syndrome measurements, where d is the distance of the surface code patch encoding the logical qubit Fowler et al. [2012]. Each round of syndrome measurements consists of a single measurement of each X and Z -type stabilizer generator of the code. Repeated rounds of syndrome measurements aid in offsetting the effects of measurement errors which corrupt the measured syndrome.

Individual stabilizer generators are measured non-destructively by coupling the relevant data qubits to a single ancilla qubit which is then measured to infer the outcome. Typically this is achieved using CX or CZ gates between the data qubits and the measurement ancilla Fowler et al. [2012] (see Figure 4). The surface code architecture allows for all stabilizer measurements in a single round to be carried out simultaneously in parallel when using two-qubit entangling gates (see Figure 5a). By mandating a specific schedule for the order in which the two-qubit gates are executed, one can avoid reducing the effective distance of the code by spreading X or Z errors along their respective logical operator directions. We refer to this circuit described using Figures 4 and 5a as the standard parity check circuit for the surface code.

Now we describe an alternative syndrome measurement circuit for the HOP surface code. We refer to this as the HOP circuit. One apparent benefit of using the multi-qubit interaction gates to perform parity checks instead of two-qubit gates is that a single parity check can effectively be performed faster. However, when using the multi-qubit interaction gates, one loses the ability to perform all parity checks in parallel as was possible with the standard circuit. Extra time before and after each multi-qubit gate is also required in order to include the twirling steps that justify our error model (Sec. 3). In Figures 5 and 6, we present a schedule for carrying out an entire round of parity checks using the HOP gates across 9 time steps.

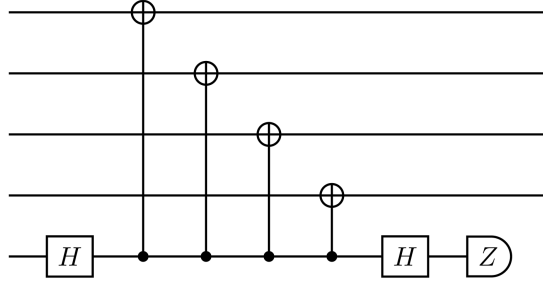


Figure 4: Standard implementation of an X -type parity check in the surface code. The first four qubits are data qubits of the code state participating in the check, and the fifth qubit is an ancilla qubit whose measurement produces the syndrome bit for this parity check. A Z -type check can be executed by replacing the CX gates with CZ gates. Note that this circuit has a time depth of 6.

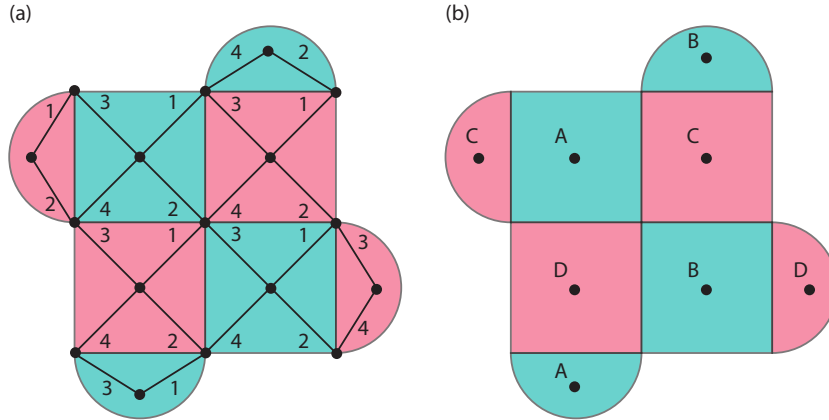


Figure 5: Schedules for surface code operation. (a) Optimal scheduling of two-qubit gates that allow simultaneous measurement of all parity checks of a distance 3 rotated surface code. Teal squares represent Z -checks, magenta squares represent X -checks, black circles on vertices represent data qubits, black circles on faces of tiles represent check qubits, and diagonal lines denote a 2-qubit gate (CX or CZ) coupling a data and check qubit. Performing the 2-qubit gates in the order indicated allows all stabilizer measurements to be carried out simultaneously while avoiding certain fault mechanisms that could reduce the effective distance of the code. (b) Scheduling of groups of parity checks carried out using multi-qubit parity check HOP gates. Groups of parity checks are carried out in the order ABCD.

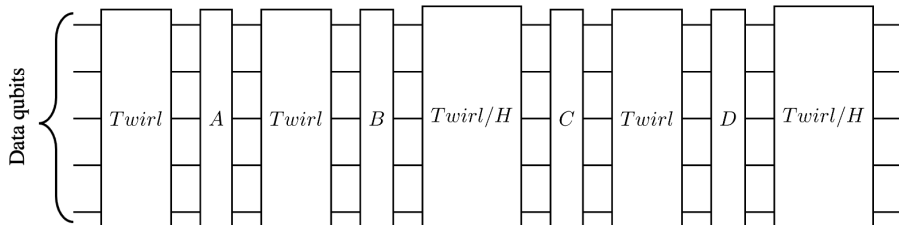


Figure 6: Circuit depicting a single round of stabilizer measurements using multi-qubit parity check gates. Blocks labeled A/B/C/D include the preparation of ancillas, coupling of the ancillas and data qubits via the appropriate multi-qubit parity check gates, and measurement of the ancillas. Blocks labeled 'Twirl' consist of random single qubit Paulis applied to the data qubits in order to justify the twirling approximation discussed in Sec. 3. Blocks labeled 'Twirl/H' also include Hadamard gates on the data qubits required in order to execute X -checks, with the assumption that the Hadamard gates can be compiled into the Twirling steps when required.

The circuit-level error models that we use to simulate error correction using either circuit are characterized by the single parameter p described in Sec. 3. Any single qubit gate location (Hadamard, Pauli twirl or idle/identity) is followed by a single qubit depolarizing channel of strength $p_1 = p/10$. Ancilla preparation and measurement locations fail with probability $p_{pm} = p/2$, where a preparation failure causes the preparation of the state orthogonal to the one intended, and a measurement failure flips the measurement outcome. For the standard circuit, the failure rate of the two-qubit gates, p_2 , is set by demanding that the process fidelity of performing a full single parity check using two-qubit gates is equal to the process fidelity of performing the parity check with the 5-qubit HOP gate. This allows us to characterize the effects of high-weight correlated errors from the HOP gates relative to the lower weight errors caused by failures of two-qubit gates. All A/B/C/D blocks in Figure 6 are followed by the correlated multi-qubit noise channels (Sec. 3) on the qubits that participated in those checks.

4.2 Simulations

We use Stim [Gidney, 2021] in order to generate Monte Carlo samples of fault patterns and their associated syndrome patterns in our syndrome measurement circuits assuming d noisy rounds of syndrome measurement followed by one perfect round to project back to the codespace [Dennis et al., 2002]. For each sample, we feed the results to a minimum-weight perfect matching (MWPM) decoder implemented in Python using PyMatching [Higgott, 2021] and record whether or not the decoder’s correction causes a logical failure by flipping a hypothetical measurement outcome of the logical Z or X operators of the code. Because Stim does not support the use of correlated Pauli channels acting on more than two qubits, the multi-qubit correlated channels are approximated in our simulations by using appropriately chosen single outcome Pauli channels as described in the appendix. Under this approximation, the probabilities of any correlated Pauli error occurring after a multi-qubit interaction gate differ from the probabilities intended by the true error model deviate only by corrections that are $O(p^3)$, which should be irrelevant in the low p regime.

In Figures 7 and 8, below, we see simulation results for the standard and HOP circuits respectively. We observe a threshold of approximately 1.25×10^{-3} for the HOP circuit and a threshold of approximately 0.79×10^{-3} for the standard circuit. As such, the HOP scheme appears to have an empirical threshold 1.5 times higher than that of the standard scheme. Note that our observed threshold for the standard scheme appears to be roughly an order of magnitude lower than the typically reported range of roughly 0.005 to 0.01 for the surface code under circuit-level noise [Stephens, 2014]. We attribute this discrepancy to our use of different failure rates for single qubit gates, multi-qubit gates, preparations, and measurements.

4.3 Resource Estimates

Here we compare the physical resources required to use either error correction scheme to implement a logical qubit encoded in a rotated surface code patch with a target logical failure rate of $p_L = 10^{-10}$. We choose this logical error rate motivated by a recent study indicating that roughly 10^{10} logical operations would be required to execute a quantum algorithm for derivative pricing in a regime where quantum advantage could be achieved Chakrabarti et al. [2021]. In order to compare resources, we fit curves describing logical failure rate as a function of physical error rate p_1 below threshold for various distances, and extrapolate those curves down to find the physical failure rate needed in order to achieve $p_L = 10^{-10}$ for each distance requiring a different number of physical qubits to implement. Linear fit data used to perform these extrapolations can be found in the appendix.

We compare estimates of two resources: physical qubit count required to implement a surface code of a distance high enough to achieve the target error rate, as well as the space-time volume (the product of physical qubit count and time steps required to complete a logical error correction cycle). In Figure 9 we see that at physical error rates closer to threshold, we can use a HOP surface code of smaller distance to achieve our target error rate than would be required using the standard surface code, as we would expect based on the fact that the HOP scheme yields a higher threshold. In terms of overall space-time volume, we see from Figure 10 that the two schemes are relatively evenly matched at higher physical error rates, but the standard scheme has an advantage at lower

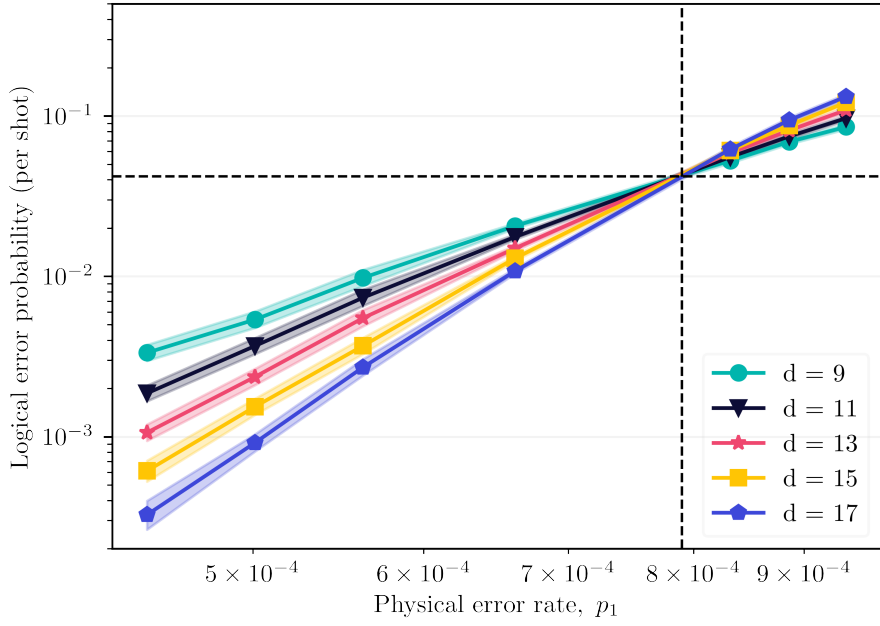


Figure 7: Logical failure rate vs physical single qubit failure rate p_1 for various distances d of the standard rotated surface code syndrome measurement circuit. Each data point reflects either 10^6 Monte Carlo trials, or the number of trials required to observe 10^4 logical failures, whichever is less. We observe that the threshold for the standard circuit under the described error model is approximately 0.79×10^{-3} . Shaded areas around curve represent a 99.9% confidence interval computed via binomial relative likelihood ratios.

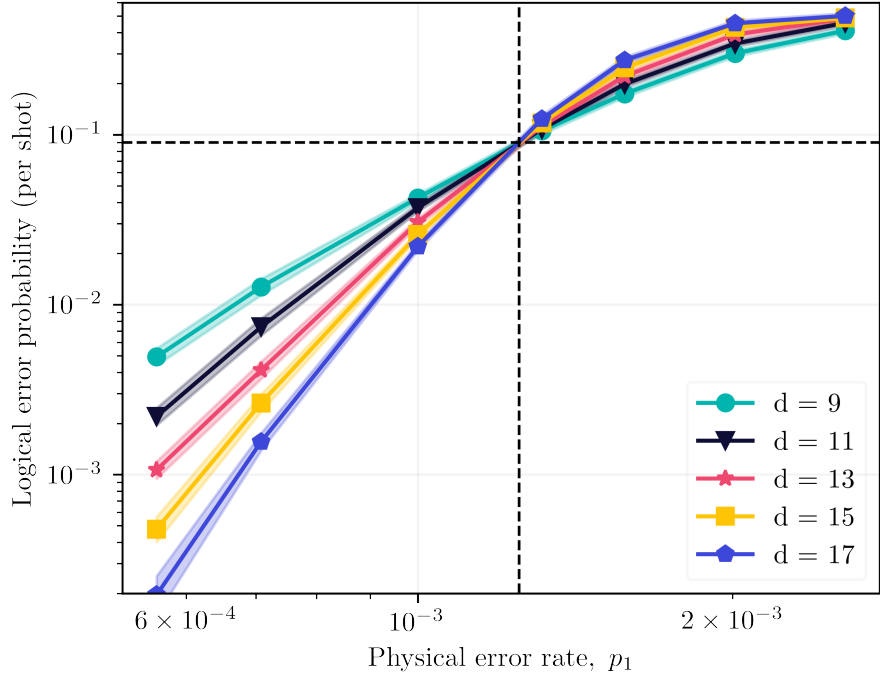


Figure 8: Logical failure rate vs physical single qubit failure rate p_1 for various distances d of the HOP syndrome measurement circuit. Each data point reflects either 10^6 Monte Carlo trials, or the number of trials required to observe 10^4 logical failures, whichever is less. We observe that the threshold for the standard circuit under the described error model is approximately 1.25×10^{-3} . Shaded areas around curve represent a 99.9% confidence interval computed via binomial relative likelihood ratios.

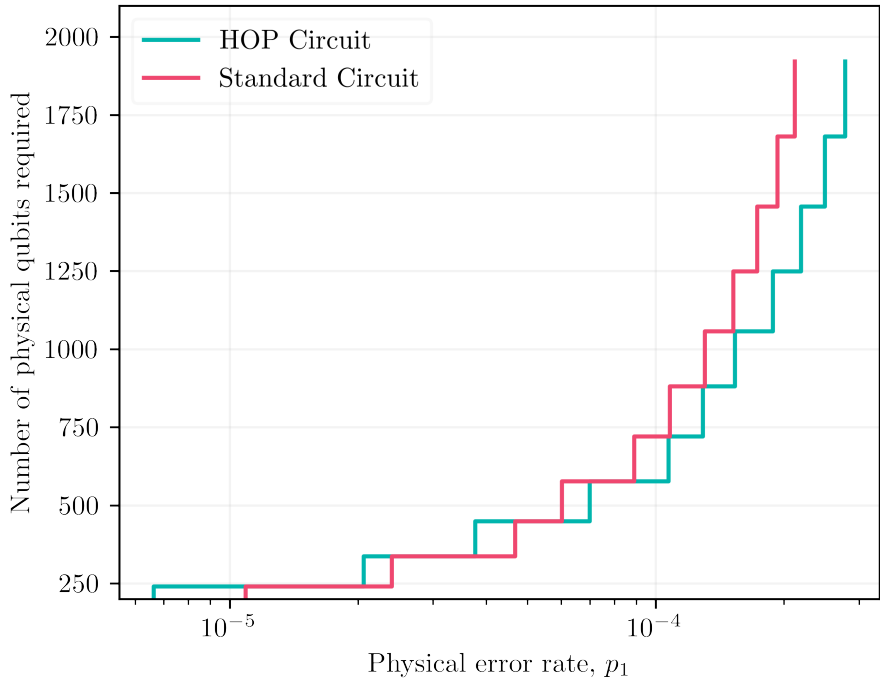


Figure 9: Comparison of the total number of physical qubits required in order to implement a logical qubit with logical error rate $p_L = 10^{-10}$ using either scheme at various physical error rates p_1 .

physical error rates. This is due to a single round of parity check measurements requiring only 6 time steps in the standard scheme while the HOP scheme requires 9.

5 Conclusions

We have presented simulated results of a surface code generated using a parity check operation defined by a strong, five-qubit dispersive ZZ interaction between data qubits and their corresponding stabilizer qubits, called the Hardware Optimized Parity (HOP) gate. We found a circuit-level error threshold for the HOP gate of approximately 1.25×10^{-3} using conservative estimates for the code construction. For realistic HOP gate parameters of $\zeta_0/2\pi = 5$ MHz, this corresponds to a threshold for decoherence rates as $T_2 = 80$ μ s, which is readily exceeded with state-of-art transmon devices [Place et al., 2021, Siddiqi, 2021]. Potential advantages are reinforced by the space-time resource estimates near the threshold, though we note a resource advantage for the standard circuit at lower physical error rates.

We believe additional improvements are likely attainable for this design. We point out that with the schedule A/B/C/D, it is possible to actuate simultaneous stabilizer measurements of the same type {A,B} and {C,D}, since the Hamiltonian for these HOP gates are mutually commuting. Moreover, an error in one qubit during the HOP gate causes, at worst, a phase flip on one of the gate targets. However, phase errors commute with the HOP Hamiltonian, meaning errors would remain local during simultaneous HOP gates, even though data qubits undergo multiple HOP gates in parallel. Investigating such optimizations is left for future work.

Further one can imagine extending HOP gate type calibration and analysis to larger subsets of the code. For example, one could design and calibrate a 13-qubit operator to perform all the ABCD steps of Figure 5b in one operator. This would push the limits of today’s calibration, but could be feasible in the future.

Another intriguing possibility is operating the HOP based surface code at a static flux bias $\zeta(t) = \zeta_0$. Removing active controls for entangling gates would address a major challenge towards managing the thermal heat load of large-scale superconducting processors—approximately halving the dissipation at cryogenic temperatures. First, for systems running HOP gates exclusively

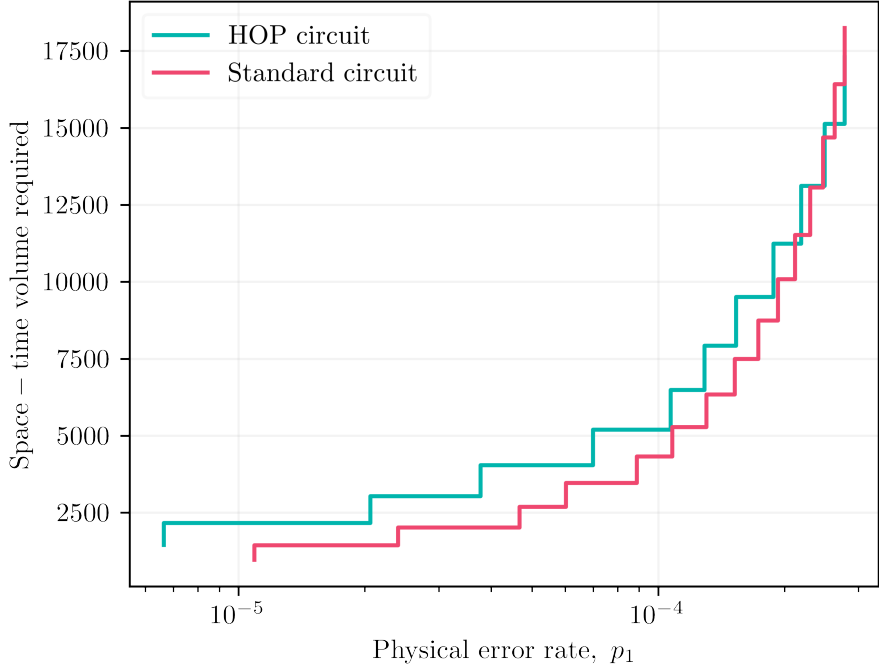


Figure 10: Comparison of the overall space-time volume required in order to implement a single error correction cycle of a logical qubit with logical error rate $p_L = 10^{-10}$ using either scheme at various physical error rates p_1 .

for entanglement, all DC current bias can be delivered over twisted pair (TwP) superconducting wire (for instance, niobium-titanium alloys) instead of coaxial signal delivery, which is otherwise standard for high-bandwidth two-qubit gate signals [DiCarlo et al., 2009]. This rewiring, alone, would amount to a hundredfold reduction in passive heat load at the coldest stages of the dilution refrigerator for two-qubit signals [Krinner et al., 2019, Hollister et al., 2021], eliminating approximately 40% of the total estimated thermal budget [Krinner et al., 2019]. Moreover, another 10% of total thermal budget would be saved by eliminating the active heat load from fast two-qubit gate pulses [Krinner et al., 2019]. Maintaining an equal thermal footprint while doubling the number of physical qubits could prove to be a leading motivation for HOP gates. Note that Hadamard gates in this architecture must be done unconditionally on the state of other qubits in the presence of the ZZ interaction, which has been demonstrated with high-fidelity for analogous experiments with strong-dispersive interactions in cavity-transmon systems using either large bandwidth control [Kirchmair et al., 2013] or optimal control [Heeres et al., 2015]. Exploring these ideas with near-term hardware will be an essential step in understanding the implications.

6 Acknowledgements

This work was jointly sponsored by Rigetti Computing and Goldman Sachs. We thank Stefano Poletto and Angela Chen for their useful input on hardware parameters that helped with calculations of next-nearest neighbor interactions. We thank Craig Gidney and Oscar Higgott for assistance in troubleshooting the use of Stim and PyMatching respectively. We thank Michael Beverland for valuable feedback on early simulation results. Results in this work was made possible using a combination of open-source software utilities as cited in the main text.

A Parameters for nearest neighbor and next-nearest neighbor ZZ couplings for 5-qubit system

The nearest neighbor and next-nearest neighbor ZZ couplings are calculated by diagonalizing the full five-qubit Hamiltonian given by Eq. (2). We used realistic parameters [Sete et al. \[2021\]](#) for asymmetric tunable coupler and parameters of the qubits for numerical diagonalization to computed ZZ couplings.

The nearest neighbor ZZ couplings for between the stabilizer and data qubits are

$$\zeta_{01} = \tilde{\omega}_{|10100\rangle} + \tilde{\omega}_{|00000\rangle} - \tilde{\omega}_{|10000\rangle} - \tilde{\omega}_{|00100\rangle}, \quad (16)$$

$$\zeta_{02} = \tilde{\omega}_{|01100\rangle} + \tilde{\omega}_{|00000\rangle} - \tilde{\omega}_{|01000\rangle} - \tilde{\omega}_{|00100\rangle}, \quad (17)$$

$$\zeta_{03} = \tilde{\omega}_{|00110\rangle} + \tilde{\omega}_{|00000\rangle} - \tilde{\omega}_{|00100\rangle} - \tilde{\omega}_{|00010\rangle}, \quad (18)$$

$$\zeta_{04} = \tilde{\omega}_{|00101\rangle} + \tilde{\omega}_{|00000\rangle} - \tilde{\omega}_{|00100\rangle} - \tilde{\omega}_{|00001\rangle} \quad (19)$$

and the next-nearest neighbor couplings between data qubits are given by

$$\zeta_{12} = \tilde{\omega}_{|11000\rangle} + \tilde{\omega}_{|00000\rangle} - \tilde{\omega}_{|10000\rangle} - \tilde{\omega}_{|01000\rangle}, \quad (20)$$

$$\zeta_{13} = \tilde{\omega}_{|10010\rangle} + \tilde{\omega}_{|00000\rangle} - \tilde{\omega}_{|10000\rangle} - \tilde{\omega}_{|00010\rangle}, \quad (21)$$

$$\zeta_{14} = \tilde{\omega}_{|10001\rangle} + \tilde{\omega}_{|00000\rangle} - \tilde{\omega}_{|10000\rangle} - \tilde{\omega}_{|00001\rangle}, \quad (22)$$

$$\zeta_{23} = \tilde{\omega}_{|01010\rangle} + \tilde{\omega}_{|00000\rangle} - \tilde{\omega}_{|01000\rangle} - \tilde{\omega}_{|00010\rangle}, \quad (23)$$

$$\zeta_{24} = \tilde{\omega}_{|01001\rangle} + \tilde{\omega}_{|00000\rangle} - \tilde{\omega}_{|01000\rangle} - \tilde{\omega}_{|00001\rangle}, \quad (24)$$

$$\zeta_{34} = \tilde{\omega}_{|00011\rangle} + \tilde{\omega}_{|00000\rangle} - \tilde{\omega}_{|00010\rangle} - \tilde{\omega}_{|00001\rangle}. \quad (25)$$

parameter	value
$g_{0j}/2\pi$	-8 MHz
$g_{0c_1}/2\pi$	130 MHz
$g_{0c_2}/2\pi$	132 MHz
$g_{0c_3}/2\pi$	-112 MHz
$g_{0c_4}/2\pi$	-130 MHz
$g_{1c_1}/2\pi$	-149.5 MHz
$g_{2c_2}/2\pi$	-134.5 MHz
$g_{3c_3}/2\pi$	134.5 MHz
$g_{4c_4}/2\pi$	143.0 MHz

Table 1: Stabilizer-data qubit couplings and qubit-tunable coupler couplings used in the numerical diagonalization of the 5-qubit Hamiltonian (2) for computing the ZZ couplings.

B Approximating a Correlated Pauli Channel

As discussed in Sec. 3, the 5Q and 3Q interactions are represented in our circuit-level error model via perfect entangling gates followed by a correlated 5Q or 3Q Pauli channel:

$$\mathcal{E}_{5/3}(\rho) = \sum_{A \in \mathcal{P}_{5/3}} p_A A \rho A^\dagger, \quad (26)$$

where p_A is the probability that pauli $A \in \mathcal{P}_{5/3}$ occurs. Recall that the characteristic parameter p of the channel describes the strength of the noise in the system, and that $p > p_A$ for any A .

Stim, however, does not support the use of correlated Pauli channels with more than two outcomes beyond two qubits. In this appendix, we discuss and justify how we approximated our intended noise model using the channels that Stim natively permits. Stim allows the use of a channel that applies an arbitrary multi-qubit Pauli operator with probability p , and otherwise applies the identity, with probability $1 - p$:

$$\mathcal{E}_{A,p}(\rho) = (1 - p)\rho + pA\rho A^\dagger, \quad A \in \mathcal{P}_n \quad (27)$$

parameters	q ₀	q ₁	q ₂	q ₃	q ₄	c ₁	c ₂	c ₃	c ₄
$\omega_{\max}/2\pi(\text{GHz})$	4.0	3.85	3.80	4.15	4.20	6.7	6.7	6.7	6.7
$\omega_{\min}/2\pi(\text{GHz})$	-	-	-	-	-	4.58	4.75	4.9	4.9
$\eta_{\max}/2\pi(\text{MHz})$	185	221	190	216	220	200	200	200	200

Table 2: Frequencies and anharmonicities of the qubits and tunable couplers used in the numerical diagonalization of the 5-qubit Hamiltonian (2) for computing the ZZ couplings.

We will refer to such channels as single-outcome Pauli channels.

A simple way of approximating $\mathcal{E}_{5/3}$ is to replace it with a channel $\mathcal{E}'_{5/3}$ which sequentially applies a separate single-outcome Pauli channel \mathcal{E}_{A,p_A} for each non-trivial Pauli operator $A \in \mathcal{P}_{5/3}$ with its corresponding probability p_A . Our desired channel $\mathcal{E}_{5/3}$ applies Pauli A with probability p_A , and by comparison, our approximate channel $\mathcal{E}'_{5/3}$ will apply Pauli A with probability

$$p'_A = p_A + C'_{A,p^2} + C'_{A,p^3} + \dots + C'_{A,p^{4^{5/3}}}, \quad (28)$$

where C'_{A,p^k} is the sum of all probabilities that exactly k of the single-outcome channels of $\mathcal{E}'_{5/3}$ apply non-trivial Paulis whose product gives the Pauli A . Because $p > p_A$, we see that

$$p'_A = p_A + O(p^2). \quad (29)$$

This tells us that $\mathcal{E}'_{5/3}$ approximates $\mathcal{E}_{5/3}$ to first order in p , and could be a reasonable approximation for small values of p .

We can improve this approximation to order $O(p^2)$ with a reasonable computational overhead by computing C'_{A,p^2} for each $A \in \mathcal{P}_{5/3}$ and shifting the probabilities for each of the single-outcome Pauli channels to $p_A - C'_{A,p^2}$. We refer to the channel built with this procedure as $\mathcal{E}''_{5/3}$.

Lemma: The channel $\mathcal{E}''_{5/3}$ applies pauli A with probability $p_A + O(p^3)$.

Proof: Under the shift $p_A \rightarrow p_A - C'_{A,p^2}$, we have that the probability of applying A is

$$p''_A = p_A - C'_{A,p^2} + C''_{A,p^2} + C''_{A,p^3} + \dots + C''_{A,p^{4^{5/3}}}, \quad (30)$$

where the terms C''_{A,p^k} are defined appropriately with the shifted probabilities. Examining C''_{A,p^2} , we have that

$$C''_{A,p^2} = \sum_{B,C \text{ s.t. } BC \sim A} (p_B - C'_{B,p^2})(p_C - C'_{C,p^2}) = \sum_{B,C \text{ s.t. } BC \sim A} p_B p_C + O(p^3) = C'_{A,p^2} + O(p^3), \quad (31)$$

so that

$$p''_A = p_A - C'_{A,p^2} + C'_{A,p^2} + O(p^3) = p_A + O(p^3) \quad (32)$$

as desired.

We see, then, that allowing Stim to implement the channel $\mathcal{E}''_{5/3}$ instead of $\mathcal{E}_{5/3}$ should not have a meaningful impact on simulations at low p .

C Linear Fit Data for Error Correction Simulations

In order to estimate the code distances required in order to achieve target physical error rates outside of the simulated regime, we perform linear fits in logarithmic space to extract the logical error rate's functional dependence on the code distance d and physical error rate p_1 . We use the simple heuristic [Fowler et al. \[2012\]](#)

$$p_L(p_1, d) = c(d)p_1^{m(d)}, \quad (33)$$

where we expect $m(d)$ to be a linear function of d and $c(d)$ to be an exponential function of d . Tables 3 and 4 list the fit parameters obtained for the HOP and standard schemes respectively, while Figures 11 and 12 show the lines fitted to the data points.

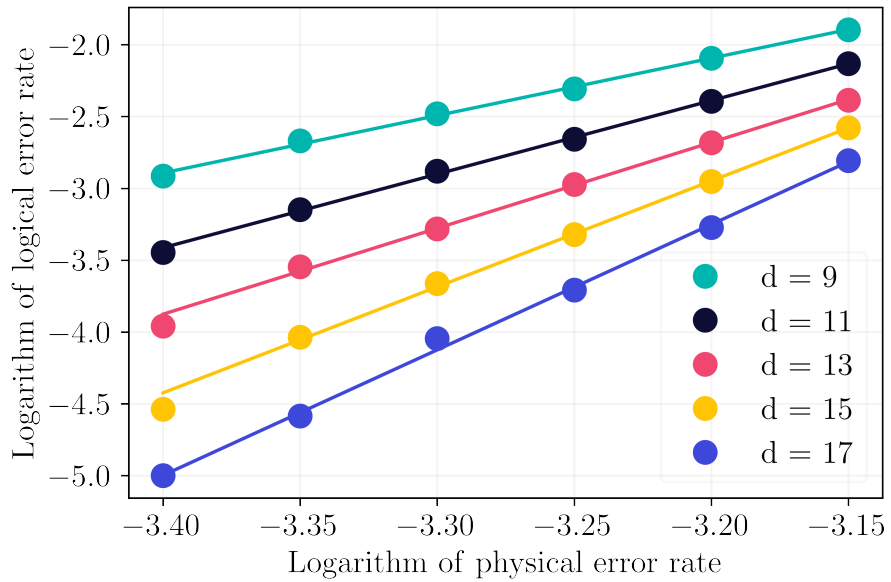


Figure 11: Linear fits of lower p_1 simulation data for the HOP scheme.

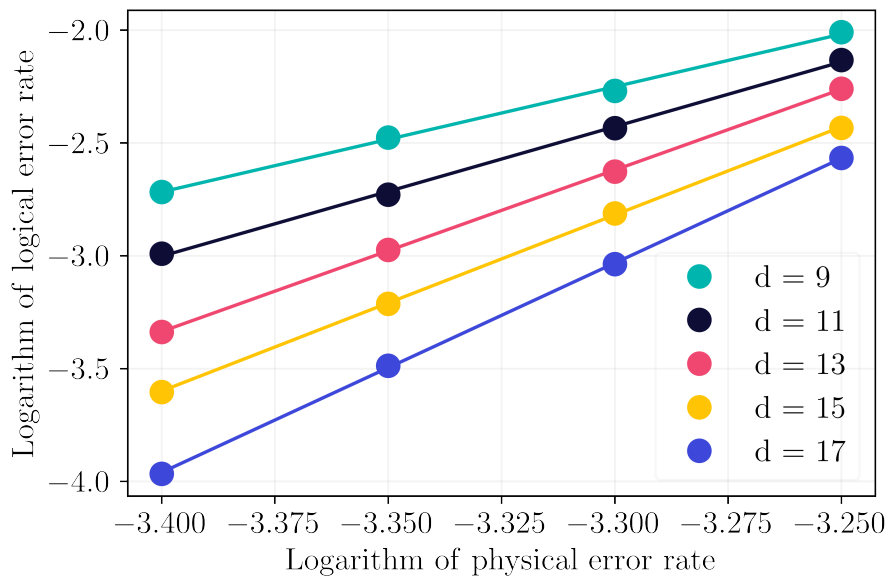


Figure 12: Linear fits of lower p_1 simulation data for the standard scheme.

Table 3: Table describing fit parameters obtained from linear regression for the HOP scheme.

d	$\log c(d)$	$m(d)$
9	10.69	3.99
11	14.00	5.12
13	16.46	5.98
15	20.65	7.37
17	24.70	8.73
19	26.62	9.41
21	28.60	10.11

Table 4: Table describing fit parameters obtained from linear regression for the standard scheme.

d	$\log c(d)$	$m(d)$
9	13.13	4.66
11	16.51	5.74
13	21.00	7.16
15	22.93	7.80
17	27.58	9.27

By performing linear regression on the data points obtained for $m(d)$ and $\log c(d)$, we can estimate $m(d)$ and $\log c(d)$ for d larger than we were able to practically simulate, and use these extrapolated values to produce Figures 9 and 10 in the main text. We found the lines of best fit for $m(d)$ for each scheme to be

$$m_{HOP}(d) = 0.53d - 0.71 \quad (34)$$

and

$$m_{Std}(d) = 0.56d - 0.406 \quad (35)$$

whereas the lines of best fit for $\log c(d)$ were found to be

$$\log c_{HOP}(d) = 1.56d - 3.11 \quad (36)$$

and

$$\log c_{Std}(d) = 1.77d - 2.73. \quad (37)$$

References

S. B. Bravyi and A. Yu. Kitaev. Quantum codes on a lattice with boundary, 1998. URL <https://arxiv.org/abs/quant-ph/9811052>.

Eric Dennis, Alexei Kitaev, Andrew Landahl, and John Preskill. Topological quantum memory. *Journal of Mathematical Physics*, 43(9):4452–4505, sep 2002. DOI: [10.1063/1.1499754](https://doi.org/10.1063/1.1499754). URL <https://doi.org/10.1063%2F1.1499754>.

Austin G. Fowler, Matteo Mariantoni, John M. Martinis, and Andrew N. Cleland. Surface codes: Towards practical large-scale quantum computation. *Physical Review A*, 86(3), sep 2012. DOI: [10.1103/physreva.86.032324](https://doi.org/10.1103/physreva.86.032324). URL <https://doi.org/10.1103%2Fphysreva.86.032324>.

Sergey Bravyi, Guillaume Duclos-Cianci, David Poulin, and Martin Suchara. Subsystem surface codes with three-qubit check operators, 2012. URL <https://arxiv.org/abs/1207.1443>.

Barbara M. Terhal. Quantum error correction for quantum memories. *Reviews of Modern Physics*, 87(2):307–346, apr 2015. DOI: [10.1103/revmodphys.87.307](https://doi.org/10.1103/revmodphys.87.307). URL <https://doi.org/10.1103%2Frevmodphys.87.307>.

Muyuan Li, Daniel Miller, Michael Newman, Yukai Wu, and Kenneth R. Brown. 2d compass codes. *Phys. Rev. X*, 9:021041, May 2019. DOI: [10.1103/PhysRevX.9.021041](https://doi.org/10.1103/PhysRevX.9.021041). URL <https://link.aps.org/doi/10.1103/PhysRevX.9.021041>.

J. Kelly, R. Barends, A. G. Fowler, A. Megrant, E. Jeffrey, T. C. White, D. Sank, J. Y. Mutus, B. Campbell, Yu Chen, Z. Chen, B. Chiaro, A. Dunsworth, I.-C. Hoi, C. Neill, P. J. J. O’Malley, C. Quintana, P. Roushan, A. Vainsencher, J. Wenner, A. N. Cleland, and John M. Martinis. State preservation by repetitive error detection in a superconducting quantum circuit. *Nature*, 519(7541):66–69, mar 2015. DOI: [10.1038/nature14270](https://doi.org/10.1038/nature14270). URL <https://doi.org/10.1038/nature14270>.

Christian Kraglund Andersen, Ants Remm, Stefania Lazar, Sebastian Krinner, Nathan Lacroix, Graham J. Norris, Mihai Gabureac, Christopher Eichler, and Andreas Wallraff. Repeated quantum error detection in a surface code. *Nature Physics*, 16(8):875–880, jun 2020. DOI: [10.1038/s41567-020-0920-y](https://doi.org/10.1038/s41567-020-0920-y). URL <https://doi.org/10.1038/s41567-020-0920-y>.

J. F. Marques, B. M. Varbanov, M. S. Moreira, H. Ali, N. Muthusubramanian, C. Zacharidis, F. Battistel, M. Beekman, N. Haider, W. Vlothuizen, A. Bruno, B. M. Terhal, and L. DiCarlo. Logical-qubit operations in an error-detecting surface code. *Nature Physics*, 18(1):80–86, dec 2021. DOI: [10.1038/s41567-021-01423-9](https://doi.org/10.1038/s41567-021-01423-9). URL <https://doi.org/10.1038/s41567-021-01423-9>.

Zijun Chen, Kevin J. Satzinger, Juan Atalaya, Alexander N. Korotkov, Andrew Dunsworth, Daniel Sank, Chris Quintana, Matt McEwen, Rami Barends, Paul V. Klimov, Sabrina Hong, Cody Jones, Andre Petukhov, Dvir Kafri, Sean Demura, Brian Burkett, Craig Gidney, Austin G. Fowler, Harald Putterman, Igor Aleiner, Frank Arute, Kunal Arya, Ryan Babbush, Joseph C. Bardin, Andreas Bengtsson, Alexandre Bourassa, Michael Broughton, Bob B. Buckley, David A. Buell, Nicholas Bushnell, Benjamin Chiaro, Roberto Collins, William Courtney, Alan R. Derk, Daniel Eppens, Catherine Erickson, Edward Farhi, Brooks Foxen, Marissa Giustina, Jonathan A. Gross, Matthew P. Harrigan, Sean D. Harrington, Jeremy Hilton, Alan Ho, Trent Huang, William J. Huggins, L. B. Ioffe, Sergei V. Isakov, Evan Jeffrey, Zhang Jiang, Kostyantyn Kechedzhi, Seon Kim, Fedor Kostritsa, David Landhuis, Pavel Laptev, Erik Lucero, Orion Martin, Jarrod R. McClean, Trevor McCourt, Xiao Mi, Kevin C. Miao, Masoud Mohseni, Wojciech Mruczkiewicz, Josh Mutus, Ofer Naaman, Matthew Neeley, Charles Neill, Michael Newman, Murphy Yuezhen Niu, Thomas E. O’Brien, Alex Opremcak, Eric Ostby, Bálint Pató, Nicholas Redd, Pedram Roushan, Nicholas C. Rubin, Vladimir Shvarts, Doug Strain, Marco Szalay, Matthew D. Trevithick, Benjamin Villalonga, Theodore White, Z. Jamie Yao, Ping Yeh, Adam Zalcman, Hartmut Neven, Sergio Boixo, Vadim Smelyanskiy, Yu Chen, Anthony Megrant, and Julian Kelly. Exponential suppression of bit or phase flip errors with repetitive error correction, 2021. URL <https://arxiv.org/abs/2102.06132>.

Sebastian Krinner, Nathan Lacroix, Ants Remm, Agustin Di Paolo, Elie Genois, Catherine Leroux, Christoph Hellings, Stefania Lazar, Francois Swiadek, Johannes Herrmann, Graham J. Norris, Christian Kraglund Andersen, Markus Müller, Alexandre Blais, Christopher Eichler, and Andreas Wallraff. Realizing repeated quantum error correction in a distance-three surface code. *Nature*, 605(7911):669–674, may 2022. DOI: [10.1038/s41586-022-04566-8](https://doi.org/10.1038/s41586-022-04566-8). URL <https://doi.org/10.1038/s41586-022-04566-8>.

Marios H. Michael, Matti Silveri, R. T. Brierley, Victor V. Albert, Juha Salmilehto, Liang Jiang, and S. M. Girvin. New class of quantum error-correcting codes for a bosonic mode. *Phys. Rev. X*, 6:031006, Jul 2016. DOI: [10.1103/PhysRevX.6.031006](https://doi.org/10.1103/PhysRevX.6.031006). URL <https://link.aps.org/doi/10.1103/PhysRevX.6.031006>.

David K. Tuckett, Stephen D. Bartlett, and Steven T. Flammia. Ultrahigh error threshold for surface codes with biased noise. *Physical Review Letters*, 120(5), jan 2018. DOI: [10.1103/physrevlett.120.050505](https://doi.org/10.1103/physrevlett.120.050505). URL <https://doi.org/10.1103/physrevlett.120.050505>.

Mazyar Mirrahimi, Zaki Leghtas, Victor V Albert, Steven Touzard, Robert J Schoelkopf, Liang Jiang, and Michel H Devoret. Dynamically protected cat-qubits: a new paradigm for universal quantum computation. *New Journal of Physics*, 16(4):045014, apr 2014. DOI: [10.1088/1367-2630/16/4/045014](https://doi.org/10.1088/1367-2630/16/4/045014). URL <https://doi.org/10.1088/1367-2630/16/4/045014>.

Baptiste Royer, Shruti Puri, and Alexandre Blais. Qubit parity measurement by parametric driving in circuit QED. *Science Advances*, 4(11), nov 2018. DOI: [10.1126/sciadv.aau1695](https://doi.org/10.1126/sciadv.aau1695). URL <https://doi.org/10.1126/sciadv.aau1695>.

Christopher Chamberland, Kyungjoo Noh, Patricio Arrangoiz-Arriola, Earl T. Campbell, Connor T. Hann, Joseph Iverson, Harald Putterman, Thomas C. Bohdanowicz, Steven T. Flammia, Andrew Keller, Gil Refael, John Preskill, Liang Jiang, Amir H. Safavi-Naeini, Oskar Painter,

and Fernando G.S.L. Brandão. Building a fault-tolerant quantum computer using concatenated cat codes. *PRX Quantum*, 3(1), feb 2022. DOI: [10.1103/prxquantum.3.010329](https://doi.org/10.1103/prxquantum.3.010329). URL <https://doi.org/10.1103%2Fprxquantum.3.010329>.

M. D. Reed, L. DiCarlo, S. E. Nigg, L. Sun, L. Frunzio, S. M. Girvin, and R. J. Schoelkopf. Realization of three-qubit quantum error correction with superconducting circuits. *Nature*, 482(7385):382–385, feb 2012. DOI: [10.1038/nature10786](https://doi.org/10.1038/nature10786). URL <https://doi.org/10.1038%2Fnature10786>.

Nissim Ofek, Andrei Petrenko, Reinier Heeres, Philip Reinhold, Zaki Leghtas, Brian Vlastakis, Yehan Liu, Luigi Frunzio, S. M. Girvin, Liang Jiang, Mazyar Mirrahimi, M. H. Devoret, and R. J. Schoelkopf. Demonstrating quantum error correction that extends the lifetime of quantum information, 2016. URL <https://arxiv.org/abs/1602.04768>.

M. Cerezo, Andrew Arrasmith, Ryan Babbush, Simon C. Benjamin, Suguru Endo, Keisuke Fujii, Jarrod R. McClean, Kosuke Mitarai, Xiao Yuan, Lukasz Cincio, and Patrick J. Coles. Variational quantum algorithms. *Nature Reviews Physics*, 3(9):625–644, aug 2021. DOI: [10.1038/s42254-021-00348-9](https://doi.org/10.1038/s42254-021-00348-9). URL <https://doi.org/10.1038%2Fs42254-021-00348-9>.

B. Foxen, C. Neill, A. Dunsworth, P. Roushan, B. Chiaro, A. Megrant, J. Kelly, Zijun Chen, K. Satzinger, R. Barends, F. Arute, K. Arya, R. Babbush, D. Bacon, J. C. Bardin, S. Boixo, D. Buell, B. Burkett, Yu Chen, R. Collins, E. Farhi, A. Fowler, C. Gidney, M. Giustina, R. Graff, M. Harrigan, T. Huang, S. V. Isakov, E. Jeffrey, Z. Jiang, D. Kafri, K. Kechedzhi, P. Klimov, A. Korotkov, F. Kostritsa, D. Landhuis, E. Lucero, J. McClean, M. McEwen, X. Mi, M. Mohseni, J. Y. Mutus, O. Naaman, M. Neeley, M. Niu, A. Petukhov, C. Quintana, N. Rubin, D. Sank, V. Smelyanskiy, A. Vainsencher, T. C. White, Z. Yao, P. Yeh, A. Zalcman, H. Neven, and J. M. Martinis and. Demonstrating a continuous set of two-qubit gates for near-term quantum algorithms. *Physical Review Letters*, 125(12), sep 2020. DOI: [10.1103/physrevlett.125.120504](https://doi.org/10.1103/physrevlett.125.120504). URL <https://doi.org/10.1103%2Fphysrevlett.125.120504>.

M. S. Blok, V. V. Ramasesh, T. Schuster, K. O’Brien, J. M. Kreikebaum, D. Dahlen, A. Morvan, B. Yoshida, N. Y. Yao, and I. Siddiqi. Quantum information scrambling on a superconducting qutrit processor. *Physical Review X*, 11(2), apr 2021. DOI: [10.1103/physrevx.11.021010](https://doi.org/10.1103/physrevx.11.021010). URL <https://doi.org/10.1103%2Fphysrevx.11.021010>.

Nathan Lacroix, Christoph Hellings, Christian Kraglund Andersen, Agustin Di Paolo, Ants Remm, Stefania Lazar, Sebastian Krinner, Graham J. Norris, Mihai Gabureac, Johannes Heinsoo, Alexandre Blais, Christopher Eichler, and Andreas Wallraff. Improving the performance of deep quantum optimization algorithms with continuous gate sets. *PRX Quantum*, 1(2), oct 2020. DOI: [10.1103/prxquantum.1.020304](https://doi.org/10.1103/prxquantum.1.020304). URL <https://doi.org/10.1103%2Fprxquantum.1.020304>.

Alexander D. Hill, Mark J. Hodson, Nicolas Didier, and Matthew J. Reagor. Realization of arbitrary doubly-controlled quantum phase gates, 2021. URL <https://arxiv.org/abs/2108.01652>.

Craig Gidney. A pair measurement surface code on pentagons, 2022. URL <https://arxiv.org/abs/2206.12780>.

Rui Chao, Michael E. Beverland, Nicolas Delfosse, and Jeongwan Haah. Optimization of the surface code design for majorana-based qubits. *Quantum*, 4:352, oct 2020. DOI: [10.22331/q-2020-10-28-352](https://doi.org/10.22331/q-2020-10-28-352). URL <https://doi.org/10.22331%2Fq-2020-10-28-352>.

Klaus Mølmer and Anders Sørensen. Multiparticle entanglement of hot trapped ions. *Phys. Rev. Lett.*, 82:1835–1838, Mar 1999. DOI: [10.1103/PhysRevLett.82.1835](https://doi.org/10.1103/PhysRevLett.82.1835). URL <https://link.aps.org/doi/10.1103/PhysRevLett.82.1835>.

Alexander Erhard, Hendrik Poulsen Nautrup, Michael Meth, Lukas Postler, Roman Stricker, Martin Stadler, Vlad Negnevitsky, Martin Ringbauer, Philipp Schindler, Hans J. Briegel, Rainer Blatt, Nicolai Friis, and Thomas Monz. Entangling logical qubits with lattice surgery. *Nature*, 589(7841):220–224, jan 2021. DOI: [10.1038/s41586-020-03079-6](https://doi.org/10.1038/s41586-020-03079-6). URL <https://doi.org/10.1038%2Fs41586-020-03079-6>.

D. Nigg, M. Müller, E. A. Martinez, P. Schindler, M. Hennrich, T. Monz, M. A. Martin-Delgado, and R. Blatt. Quantum computations on a topologically encoded qubit. *Science*, 345(6194):302–305, jul 2014. DOI: [10.1126/science.1253742](https://doi.org/10.1126/science.1253742). URL <https://doi.org/10.1126%2Fscience.1253742>.

A. Bermudez, X. Xu, R. Nigmatullin, J. O’Gorman, V. Negnevitsky, P. Schindler, T. Monz, U. G. Poschinger, C. Hempel, J. Home, F. Schmidt-Kaler, M. Biercuk, R. Blatt, S. Benjamin, and M. Müller. Assessing the progress of trapped-ion processors towards fault-tolerant quantum

computation. *Physical Review X*, 7(4), dec 2017. DOI: [10.1103/physrevx.7.041061](https://doi.org/10.1103/physrevx.7.041061). URL <https://doi.org/10.1103/physrevx.7.041061>.

David Schwerdt, Yotam Shapira, Tom Manovitz, and Roee Ozeri. Comparing two-qubit and multiqubit gates within the toric code. *Physical Review A*, 105(2), feb 2022. DOI: [10.1103/physreva.105.022612](https://doi.org/10.1103/physreva.105.022612). URL <https://doi.org/10.1103/physreva.105.022612>.

Frank Arute, Kunal Arya, Ryan Babbush, Dave Bacon, Joseph C. Bardin, Rami Barends, Rupak Biswas, Sergio Boixo, Fernando G. S. L. Brandao, David A. Buell, Brian Burkett, Yu Chen, Zijun Chen, Ben Chiaro, Roberto Collins, William Courtney, Andrew Dunsworth, Edward Farhi, Brooks Foxen, Austin Fowler, Craig Gidney, Marissa Giustina, Rob Graff, Keith Guerin, Steve Habegger, Matthew P. Harrigan, Michael J. Hartmann, Alan Ho, Markus Hoffmann, Trent Huang, Travis S. Humble, Sergei V. Isakov, Evan Jeffrey, Zhang Jiang, Dvir Kafri, Kostyantyn Kechedzhi, Julian Kelly, Paul V. Klimov, Sergey Knysh, Alexander Korotkov, Fedor Kostritsa, David Landhuis, Mike Lindmark, Erik Lucero, Dmitry Lyakh, Salvatore Mandrà, Jarrod R. McClean, Matthew McEwen, Anthony Megrant, Xiao Mi, Kristel Michelsen, Masoud Mohseni, Josh Mutus, Ofer Naaman, Matthew Neeley, Charles Neill, Murphy Yuezhen Niu, Eric Ostby, Andre Petukhov, John C. Platt, Chris Quintana, Eleanor G. Rieffel, Pedram Roushan, Nicholas C. Rubin, Daniel Sank, Kevin J. Satzinger, Vadim Smelyanskiy, Kevin J. Sung, Matthew D. Trevithick, Amit Vainsencher, Benjamin Villalonga, Theodore White, Z. Jamie Yao, Ping Yeh, Adam Zalcman, Hartmut Neven, and John M. Martinis. Quantum supremacy using a programmable superconducting processor. *Nature*, 574(7779):505–510, Oct 2019. ISSN 1476-4687. DOI: [10.1038/s41586-019-1666-5](https://doi.org/10.1038/s41586-019-1666-5). URL <https://doi.org/10.1038/s41586-019-1666-5>.

Youngkyu Sung, Leon Ding, Jochen Braumüller, Antti Vepsäläinen, Bharath Kannan, Morten Kjaergaard, Ami Greene, Gabriel O. Samach, Chris McNally, David Kim, Alexander Melville, Bethany M. Niedzielski, Mollie E. Schwartz, Jonilyn L. Yoder, Terry P. Orlando, Simon Gustavsson, and William D. Oliver. Realization of high-fidelity cz and zz -free $iswap$ gates with a tunable coupler. *Phys. Rev. X*, 11:021058, Jun 2021. DOI: [10.1103/PhysRevX.11.021058](https://doi.org/10.1103/PhysRevX.11.021058). URL <https://link.aps.org/doi/10.1103/PhysRevX.11.021058>.

Eyob A. Sete, Angela Q. Chen, Riccardo Manenti, Shobhan Kulshreshtha, and Stefano Poletto. Floating tunable coupler for scalable quantum computing architectures. *Phys. Rev. Applied*, 15: 064063, Jun 2021. DOI: [10.1103/PhysRevApplied.15.064063](https://doi.org/10.1103/PhysRevApplied.15.064063). URL <https://link.aps.org/doi/10.1103/PhysRevApplied.15.064063>.

Shouvanik Chakrabarti, Rajiv Krishnakumar, Guglielmo Mazzola, Nikitas Stamatopoulos, Stefan Woerner, and William J. Zeng. A threshold for quantum advantage in derivative pricing. *Quantum*, 5:463, jun 2021. DOI: [10.22331/q-2021-06-01-463](https://doi.org/10.22331/q-2021-06-01-463). URL <https://doi.org/10.22331%2Fq-2021-06-01-463>.

Michael A. Nielsen and Isaac L. Chuang. *Quantum Computation and Quantum Information*. Cambridge University Press, 2000.

Alexander N. Korotkov. Error matrices in quantum process tomography, 2013. URL <https://arxiv.org/abs/1309.6405>.

Charles H. Bennett, David P. DiVincenzo, John A. Smolin, and William K. Wootters. Mixed-state entanglement and quantum error correction. *Physical Review A*, 54(5):3824–3851, November 1996a. DOI: [10.1103/PhysRevA.54.3824](https://doi.org/10.1103/PhysRevA.54.3824). URL <https://link.aps.org/doi/10.1103/PhysRevA.54.3824>. Publisher: American Physical Society.

Charles H. Bennett, Gilles Brassard, Sandu Popescu, Benjamin Schumacher, John A. Smolin, and William K. Wootters. Purification of Noisy Entanglement and Faithful Teleportation via Noisy Channels. *Physical Review Letters*, 76(5):722–725, January 1996b. DOI: [10.1103/PhysRevLett.76.722](https://doi.org/10.1103/PhysRevLett.76.722). URL <https://link.aps.org/doi/10.1103/PhysRevLett.76.722>. Publisher: American Physical Society.

Michael R. Geller and Zhongyuan Zhou. Efficient error models for fault-tolerant architectures and the Pauli twirling approximation. *Physical Review A*, 88(1):012314, July 2013. DOI: [10.1103/PhysRevA.88.012314](https://doi.org/10.1103/PhysRevA.88.012314). URL <https://link.aps.org/doi/10.1103/PhysRevA.88.012314>. Publisher: American Physical Society.

Daniel Manzano. A short introduction to the Lindblad master equation. *AIP Advances*, 10(2): 025106, February 2020. DOI: [10.1063/1.5115323](https://doi.org/10.1063/1.5115323). URL <https://aip.scitation.org/doi/10.1063/1.5115323>. Publisher: American Institute of Physics.

P. Krantz, M. Kjaergaard, F. Yan, T. P. Orlando, S. Gustavsson, and W. D. Oliver. A quantum engineer's guide to superconducting qubits. *Applied Physics Reviews*, 6(2):021318, jun 2019. DOI: 10.1063/1.5089550. URL <https://doi.org/10.1063/1.5089550>.

J. R. Johansson, P. D. Nation, and Franco Nori. QuTiP 2: A Python framework for the dynamics of open quantum systems. *Computer Physics Communications*, 184(4):1234–1240, April 2013. ISSN 0010-4655. DOI: 10.1016/j.cpc.2012.11.019. URL <https://www.sciencedirect.com/science/article/pii/S0010465512003955>.

Craig Gidney. Stim: a fast stabilizer circuit simulator. *Quantum*, 5:497, jul 2021. DOI: 10.22331/q-2021-07-06-497. URL <https://doi.org/10.22331%2Fq-2021-07-06-497>.

Oscar Higgott. Pymatching: A python package for decoding quantum codes with minimum-weight perfect matching, 2021. URL <https://arxiv.org/abs/2105.13082>.

Ashley M. Stephens. Fault-tolerant thresholds for quantum error correction with the surface code. *Physical Review A*, 89(2), feb 2014. DOI: 10.1103/physreva.89.022321. URL <https://doi.org/10.1103%2Fphysreva.89.022321>.

Alexander P. M. Place, Lila V. H. Rodgers, Pranav Mundada, Basil M. Smitham, Matthias Fitzpatrick, Zhaoqi Leng, Anjali Premkumar, Jacob Bryon, Andrei Vrajitoarea, Sara Sussman, Guangming Cheng, Trisha Madhavan, Harshvardhan K. Babla, Xuan Hoang Le, Youqi Gang, Berthold Jäck, András Gyenis, Nan Yao, Robert J. Cava, Nathalie P. de Leon, and Andrew A. Houck. New material platform for superconducting transmon qubits with coherence times exceeding 0.3 milliseconds. *Nature Communications*, 12(1), mar 2021. DOI: 10.1038/s41467-021-22030-5. URL <https://doi.org/10.1038%2Fs41467-021-22030-5>.

Irfan Siddiqi. Engineering high-coherence superconducting qubits. *Nature Reviews Materials*, 6(10):875–891, 2021. DOI: 10.1038/s41578-021-00370-4. URL <https://doi.org/10.1038/s41578-021-00370-4>.

L. DiCarlo, J. M. Chow, J. M. Gambetta, Lev S. Bishop, B. R. Johnson, D. I. Schuster, J. Majer, A. Blais, L. Frunzio, S. M. Girvin, and R. J. Schoelkopf. Demonstration of two-qubit algorithms with a superconducting quantum processor. *Nature*, 460(7252):240–244, jun 2009. DOI: 10.1038/nature08121. URL <https://doi.org/10.1038%2Fnature08121>.

S. Krinner, S. Storz, P. Kurpiers, P. Magnard, J. Heinsoo, R. Keller, J. Lütolf, C. Eichler, and A. Wallraff. Engineering cryogenic setups for 100-qubit scale superconducting circuit systems. *EPJ Quantum Technology*, 6(1), may 2019. DOI: 10.1140/epjqt/s40507-019-0072-0. URL <https://doi.org/10.1140%2Fepjqt%2Fs40507-019-0072-0>.

Matthew Hollister, Ram Dhuley, and Grzegorz Tatkowski. A large millikelvin platform at fermilab for quantum computing applications, 2021. URL <https://arxiv.org/abs/2108.10816>.

Gerhard Kirchmair, Brian Vlastakis, Zaki Leghtas, Simon E. Nigg, Hanhee Paik, Eran Ginossar, Mazyar Mirrahimi, Luigi Frunzio, S. M. Girvin, and R. J. Schoelkopf. Observation of quantum state collapse and revival due to the single-photon kerr effect. *Nature*, 495(7440):205–209, Mar 2013. ISSN 1476-4687. DOI: 10.1038/nature11902. URL <http://dx.doi.org/10.1038/nature11902>.

Reinier W. Heeres, Brian Vlastakis, Eric Holland, Stefan Krastanov, Victor V. Albert, Luigi Frunzio, Liang Jiang, and Robert J. Schoelkopf. Cavity state manipulation using photon-number selective phase gates. *Physical Review Letters*, 115(13), Sep 2015. ISSN 1079-7114. DOI: 10.1103/physrevlett.115.137002. URL <http://dx.doi.org/10.1103/PhysRevLett.115.137002>.